

Article

Stable Isotopic, Micro-FTIR, and Geochemical Characteristics of the Permian Madzaringwe Shale of Tuli Basin, South Africa: Implications for Organic-Rich Shale Provenance

George Oluwole Akintola ^{1,*}, Francis Amponsah-Dacosta ¹, Steven Rupprecht ²
and Sphiwe Emmanuel Mhlongo ¹

¹ Department of Earth Sciences, Faculty of Science, Engineering and Agriculture, University of Venda, Thohoyandou 0950, South Africa

² Department of Mining Engineering, University of Johannesburg, Johannesburg 2006, South Africa

* Correspondence: georgeakintola540@gmail.com

Abstract: The paleo-environmental setting of an organic-rich shale remains an essential controlling factor for shale reservoir distribution. The scarcity of generalised data on paleo-environment settings has been spurred using a simple investigative approach to decipher the provenance of organic-rich shale in various regions. This study investigates the organic-rich Madzaringwe shale of the Tuli Basin to reconstruct the provenance of the organic material for shale gas generation potential. Representative shale core samples were analysed for the stable isotopic fractions, functional groups, and major and trace compositions. The carbon isotopic composition, $\delta^{13}\text{C}$ value, ranging from -21.01 to -24.0% , averaging at -22.4% . Inference from the stable isotopic compositions and functional group analysis indicate Type-III kerogen prone to gas generation in the studied Madzaringwe shale. The micro-Fourier transformed infrared (micro-FTIR) analysis reveals infrared absorption peaks between 2800 and 3300 cm^{-1} wavelengths corresponding to gaseous hydrocarbon. The x-ray fluorescence (XRF) result reveals major elements comprising Al_2O_3 (29.25–29.11%), CaO (0.29–0.28%), Fe_2O_3 (1.16–1.09%), K_2O (0.97–0.98%), MgO (0.13–0.12%), Na_2O (0.12–0.09%), P_2O_5 (0.22–0.21%), SiO_2 (52.50–52.30%), and TiO_2 (1.20–1.18%). The major element ratio of $\text{Al}_2\text{O}_3/\text{TiO}_2$ values ≥ 25 indicates felsic and intermediate provenance from a terrigenous paleo-environment. In addition, laser ablation inductively coupled plasma mass spectrometry (LA-ICP-MS) reveals the trace elements in which elemental proxy of $\text{V}/(\text{V} + \text{Ni})$ with a value greater than 0.5 represent reducing environments. Furthermore, the geochemical proxies and isotopic compositions have revealed an anoxic paleo-environment for the non-marine-derived organic matter in the studied carbonaceous shale.

Keywords: stable isotopic; organic-rich shale; organic matter; provenance; Madzaringwe shale



Citation: Akintola, G.O.; Amponsah-Dacosta, F.; Rupprecht, S.; Mhlongo, S.E. Stable Isotopic, Micro-FTIR, and Geochemical Characteristics of the Permian Madzaringwe Shale of Tuli Basin, South Africa: Implications for Organic-Rich Shale Provenance. *Minerals* **2022**, *12*, 1160. <https://doi.org/10.3390/min12091160>

Academic Editors: Zhensheng Shi, Dazhong Dong, Tianqi Zhou and Ziliang Liu

Received: 12 August 2022

Accepted: 9 September 2022

Published: 14 September 2022

Publisher's Note: MDPI stays neutral with regard to jurisdictional claims in published maps and institutional affiliations.



Copyright: © 2022 by the authors. Licensee MDPI, Basel, Switzerland. This article is an open access article distributed under the terms and conditions of the Creative Commons Attribution (CC BY) license (<https://creativecommons.org/licenses/by/4.0/>).

1. Introduction

The provenance of organic-rich shale is critical to determining a favourable target for shale gas exploration, among other controlling factors. Controlling factors such as thermal maturity are important parameters for organic matter alteration to gas-prone kerogen [1,2]. However, the type and amount of organic matter in a shale vary due to geologic conditions and paleo-depositional environments [3]. Depending on the prevailing geological settings and paleo-climatic overprints, sedimentation of an organic-rich shale may occur in a marine, terrestrial, or transitional setting. Under favourable geologic and thermal conditions, organic matter from each depositional environment has various compositions, resulting in different source rock types.

Stable isotopic fractionations have demonstrated that interactions among elements of carbon, oxygen, and rocks are a significant indicator of a paleo-depositional environment for organic-rich shale rock. The organic materials that form kerogen prone to unconventional hydrocarbon have heterogeneous sources, depending on the paleo-depositional

environment. Based on a biomarker and petrographic study [4], an organic matter composed of terrigenous conifers plants and lacustrine algal has been reported to produce a Type II–III kerogen prone to oil and gas generation. Instead of shale gas, shale oil emanates from a marine-derived organic matter such as planktonic foraminifera assemblage, structureless (amorphous) and alginite [5]. These organic materials are typical of a marine paleo-depositional environment, producing kerogen Type I–II prone to oil generation [5]. Unlike the marine paleo-environment, the fluvial-deltaic settings receive organic material composed of a higher plant with well-developed vascular components due to proximity to the land, generating Type-III kerogen.

Organic substances produce characteristic stretching and bending frequencies between 400 and 4000 cm^{-1} wavelengths, showing their origin and evolution in the functional group [6]. The hydrocarbon C–H stretching vibrations have infrared absorption peaks between 2800 and 3300 cm^{-1} wavelength regions, while aromatic compounds have absorption peaks between 680 and 900 cm^{-1} wavelength regions. The FTIR data has shown to be an invaluable tool in screening aliphatic organic material, revealing geochemical characteristics such as volatile hydrocarbon, residual hydrocarbon generative potential, aliphatic organic materials, hydrogen index, and total organic carbon [6]. As it absorbs radiation, the FTIR provides information on the functional groups in the organic molecule, which helps constrain the origin of organic materials.

The elemental concentration of the geochemical composition of an organic-rich shale remains a veritable means to indicate a paleo-depositional environment. Some recent studies [7,8] have used elemental concentrations and elemental proxies for paleo-redox (Co, Cr, Mo, U, V, Re) and paleo-productivity (Sr, Ba, B, Ga, S) indicators. At the same time, some immobile elements, including La, Th, Co, Sc, Ni, Zr, and Y show varying concentrations based on the different parent rocks and tectonic settings. As a result, the elemental proxies of these immobile elements can be used to determine the origin and tectonic setting of shale.

Due to the scarcity of generalised data on the paleo-environment setting, which seems essential for shale gas potential distribution, reconstructing the provenance of organic materials with a simple investigative approach has become critical. Despite many decades of research in paleo-environmental settings [9,10], there is a scarcity in combining stable isotopic, functional and geochemical characterisation to decipher the provenance of organic-rich matter. In addition, the organic-rich Madzaringwe shale of the Tuli Basin indicates potential for shale gas generation. However, the paleo-depositional environment of organic matter preservation remains elusive. This study investigates the stable isotopic fractionations, organic functional group, and the major and trace elemental compositions of the Madzaringwe shale core samples from the Tuli Basin to reconstruct the provenance of the organic material.

2. Study Area

The Tuli Basin is a fault-controlled intracratonic depozone having sedimentation in an east–west trending orientation [11,12]. The genesis of this rift basin is assumed to be associated with the Late Carboniferous and Middle Jurassic break-up of the Gondwana Craton [13]. The Tuli Basin and the Tshipise, Ellisras, and Springbok Flats basins are deposited north of the Main Karoo Basin, representing the so-called Limpopo Karoo-age basins [14]. Meanwhile, the Tuli Basin generally consists of the glaciogenic Tshidzi, Madzaringwe, Mikambeni, Fripp, Solitude, Klopperfontein, Bosbokpoort, and Clarens Formations in chronological sequence. Among the sedimentary sequence, the Permian Madzaringwe and Mikambeni comprise significant carbonaceous shale and coal, alternating with sandstone and siltstone. However, the carbonaceous shale of the Madzaringwe Formation is of interest in this study due to its high estimated thickness varying from 60 to 150 m [15]. The study area is situated between 21°00'00" S and 22°30'00" S and longitude 28°28'00" E and 30°15'00" E, as shown in Figure 1.

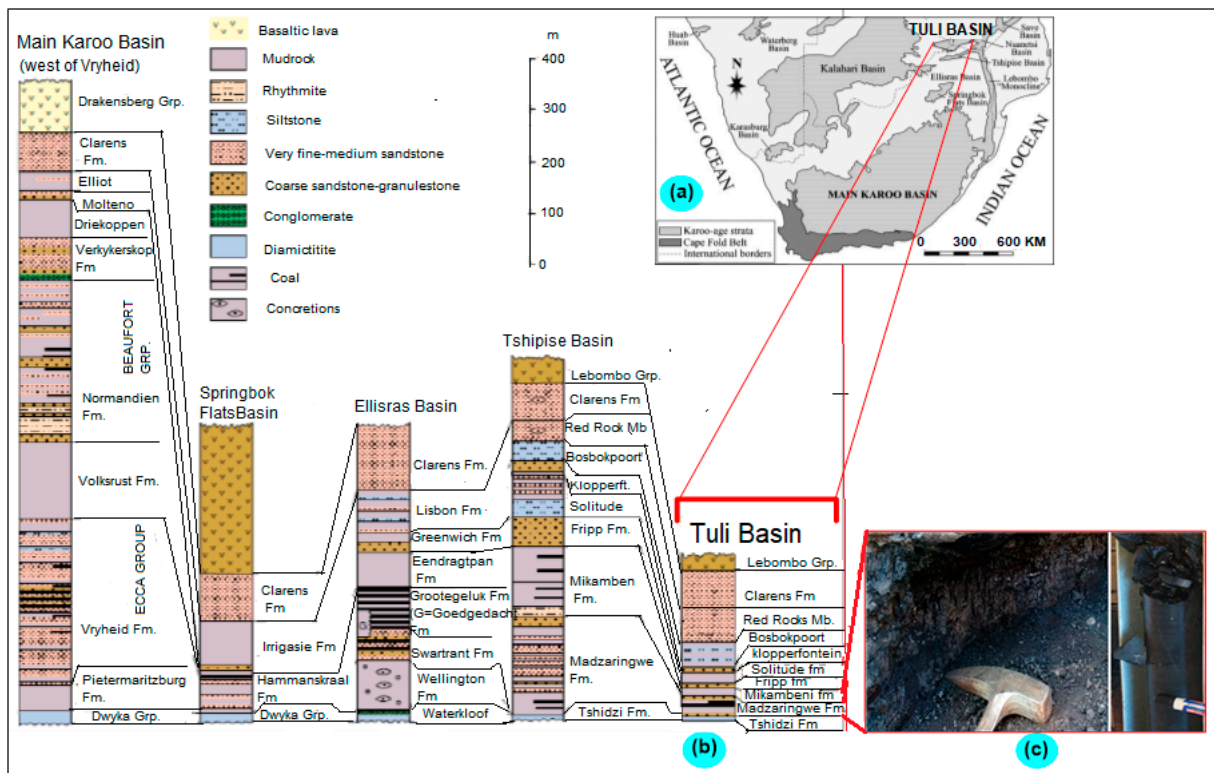


Figure 1. Study area 9 (a) Tuli Basin (b) organic-rich formation (c) organic-rich shale core sample.

The Madzaringwe shale appears to have been largely laid down by meandering rivers flowing from the northwest in the Permian period [15]. The plant materials accumulated in flood basins under cool, reducing conditions, giving rise to coal seams [16]. The Madzaringwe Formation consists of the coal-bearing strata of the Tuli Basin [17]. Although recent studies have reported varied thicknesses of coal seams, no distinct consistency is less than 20 m with six continuous coal seams interbedded with grey to black shale in a rhythmic manner [18,19]. It is not unlikely that the plant-organic-rich shale has potential for natural gas resources because the evolutionary pathway for coal and shale gas has a similar origin but different endpoints.

3. Materials and Methods

The boreholes penetrating the organic-rich Madzaringwe shale at different depths as shown in Figure 2 were analysed for stable isotopic fractions and FTIR spectra to determine organic and mineral content at various infrared wavelengths and geochemical compositions.

At the same time, the $\delta^{13}\text{C}$ and $\delta^{18}\text{O}$ values of organic-rich shale samples were measured using the Finnigan Delta^{plus} isotope ratio mass spectrometer equipped with Gas Bench II system for water equilibrium. An analytical precision $\pm 0.2\%$ was determined by repeated analyses of a standard. The dried bulk samples were dissolved in 99% H_3PO_4 , and the resulting CO_2 gas was analysed by the spectrometer [20]. The measured isotopic composition is presented as delta notation (δ) in relation to the Vienna Pee Dee Belemnite (V-PDB) standard and expressed in per mil (‰). Delta notation is defined as $\delta = [(R_{\text{sample}} - R_{\text{standard}}) / R_{\text{standard}}] \times 1000$, where R is the stable isotope ratio of $^{13}\text{C}/^{12}\text{C}$ or $^{18}\text{O}/^{16}\text{O}$.

The functional group of the studied organic-rich shale was determined by the Fourier Transform Infrared (FTIR) Alpha Bruker spectrophotometer at the University of Venda, South Africa.

The pulverised samples were placed in the measurement position of the spectrometer and scanned between the minimum and maximum wavelength range of 500 to 4000 cm^{-1} ,

respectively. The absorbance spectral depicts the crystalline phases, reflecting their functional group.

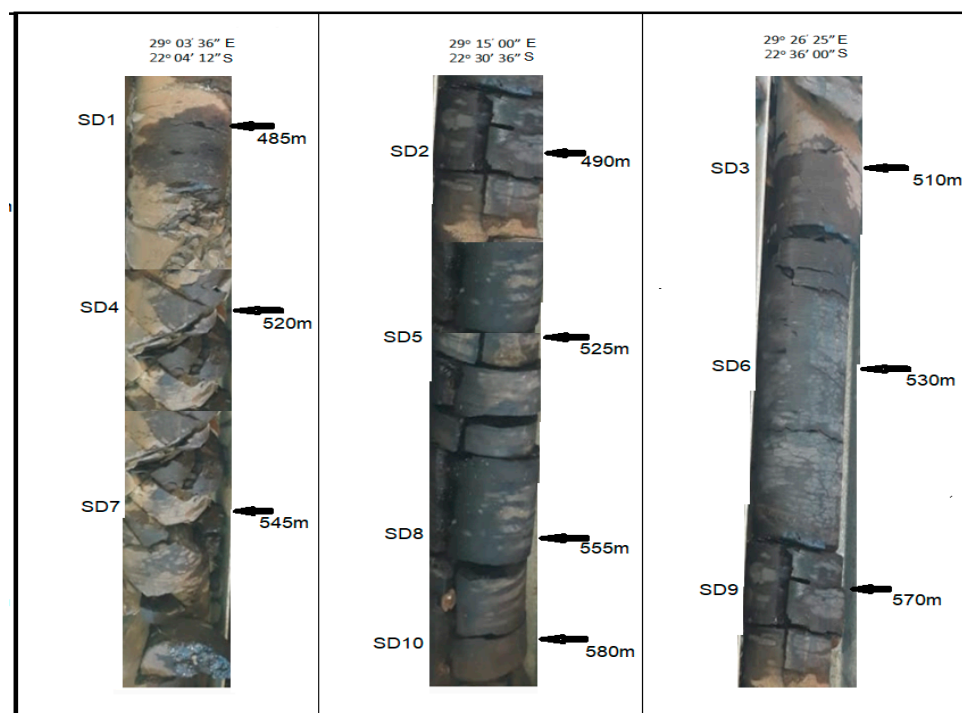


Figure 2. Organic-rich shale core samples from the study area.

The geochemical analyses of the major elements of the shale samples were quantitatively estimated using PANalytical X-ray fluorescence (XRF) at Stellenbosch University Central Analytical facilities unit, Cape Town. It is equipped with 3 kWatt Rhodium (Rh) tube and inserted glass disks containing 1 g calcined sample, 8 g flux composed of 35% alkali borate (LiBO_2) and 64.71% lithium tetraborate ($\text{Li}_2\text{B}_4\text{O}_7$) as oxidant at 1000°C . At this temperature, the weight loss or gain on ignition (LOI) includes the total volatiles content of the rock samples, including the water combined with the lattice of silicate minerals and the gain on ignition related to the oxidation of the rock mostly due to Fe. Pressed powder pellets for XRF analyses were prepared using 3 g of sample powder and 6 g of boric acid as a binder. The mixture was fused into a steel cup and pressed at a pressure of 30 tons in a hydraulic set.

Trace elements of organic-rich samples were analysed using Agilent 7700 Q ICP-MS attached to a high resolution 193 nm Excimer laser ablation system at the Central Analytical Facilities, Stellenbosch University. The pulverised samples were inserted and fixed by using a stainless-steel holder in the ablation chamber. Helium carrier gas transported the ablated material to the ICP-MS at a flow rate of 0.35 L/min, then mixed with argon (0.9 L/min) and nitrogen (0.003 L/min). For trace infusions, two spots of $104\mu\text{m}$ are ablated on each sample using a frequency of 8 Hz and fluence of $\sim 3.5\text{ J}/\text{cm}^2$. Inductively couple plasma mass spectrometry (ICP-MS) is optimised for sensitivity and low oxide ratios of less than 0.2% by tuning both the ICP and laser parameters while ablating a line on NIST612.

4. Results

The result of the geochemical compositions of the studied samples showed the presence of major oxides, as shown in Table 1. It reveals the varying presence of Al_2O_3 (29.25–29.11%), CaO (0.29–0.28%), Fe_2O_3 (1.16–1.09%), K_2O (0.97–0.98%), MgO (0.13–0.12%), Na_2O (0.12–0.09%), P_2O_5 (0.22–0.21%), SiO_2 (52.50–52.30%), and TiO_2 (1.20–1.18%) in the studied Madzaringwe samples. The relatively high value of loss-on-ignition (14.95–15.11%), which averages 15.04% in the studied shale, suggests higher carbon content. The $\text{Fe}/(\text{Fe} + \text{Mg})$

values exceeded the threshold value of 0.5 and ranged from 0.5 to 0.9, indicating the intermediate provenance consistent with the previous study [21]. The study [21] suggested a threshold limit > 0.60 as mixture of both mafic and felsic input.

Table 1. Major oxides characteristics of the studied samples.

| Sample ID | Depth (m) | Major Oxides Composition (%) | | | | | | | | | | LOI (%) | K ₂ O /Al ₂ O ₃ | Fe/(Fe + Mg) | ICV |
|-----------|-----------|--------------------------------|------|--------------------------------|------------------|------|------|-------------------|-------------------------------|------------------|------------------|---------|--|--------------|------|
| | | Al ₂ O ₃ | CaO | Fe ₂ O ₃ | K ₂ O | MgO | MnO | Na ₂ O | P ₂ O ₅ | SiO ₂ | TiO ₂ | | | | |
| SD1 | 485 | 29.17 | 0.28 | 1.10 | 0.98 | 0.12 | 0.01 | 0.11 | 0.22 | 52.26 | 1.19 | 15.04 | 0.03 | 0.90 | 0.09 |
| SD2 | 490 | 29.24 | 0.28 | 1.16 | 0.98 | 0.13 | 0.01 | 0.11 | 0.22 | 52.45 | 1.19 | 15.11 | 0.03 | 0.90 | 0.09 |
| SD3 | 510 | 29.16 | 0.28 | 1.13 | 0.98 | 0.12 | 0.01 | 0.10 | 0.22 | 52.18 | 1.20 | 15.10 | 0.03 | 0.90 | 0.09 |
| SD4 | 520 | 29.23 | 0.29 | 1.12 | 0.97 | 0.13 | 0.01 | 0.11 | 0.21 | 52.18 | 1.19 | 15.06 | 0.03 | 0.90 | 0.09 |
| SD5 | 525 | 29.19 | 0.28 | 1.13 | 0.97 | 0.13 | 0.01 | 0.10 | 0.21 | 52.26 | 1.19 | 14.95 | 0.03 | 0.90 | 0.09 |
| SD6 | 530 | 29.12 | 0.28 | 1.14 | 0.98 | 0.13 | 0.01 | 0.10 | 0.21 | 52.50 | 1.19 | 15.06 | 0.03 | 0.90 | 0.09 |
| SD7 | 545 | 29.14 | 0.29 | 1.11 | 0.97 | 0.13 | 0.01 | 0.12 | 0.21 | 52.30 | 1.18 | 14.97 | 0.03 | 0.90 | 0.09 |
| SD8 | 555 | 29.11 | 0.28 | 1.12 | 0.97 | 0.13 | 0.01 | 0.09 | 0.21 | 52.34 | 1.18 | 15.06 | 0.03 | 0.90 | 0.09 |
| SD9 | 570 | 29.25 | 0.28 | 1.12 | 0.98 | 0.13 | 0.01 | 0.10 | 0.22 | 52.25 | 1.18 | 15.03 | 0.03 | 0.90 | 0.09 |
| SD10 | 580 | 29.18 | 0.28 | 1.09 | 0.98 | 0.13 | 0.01 | 0.10 | 0.21 | 52.37 | 1.19 | 15.03 | 0.03 | 0.89 | 0.09 |
| Max | | 29.25 | 0.29 | 1.16 | 0.98 | 0.13 | 0.01 | 0.12 | 0.22 | 52.50 | 1.2 | 15.11 | | | |
| Min | | 29.11 | 0.28 | 1.09 | 0.97 | 0.12 | 0.01 | 0.09 | 0.21 | 52.18 | 1.18 | 14.95 | | | |

The trace and rare-earth element distributions (REE) in the studied samples are presented in Table 2. The trace element showed relatively high concentrations in Ba, Zr, Rb, Zn, Sr, V, and Cr with values above 50 ppm, while all other elements are lower. In the studied samples, the highest value of Barium, Ba (513.85–560.88 ppm), with an average of 545.77 ppm, suggests the dissolution of mineral barite in the black shale by action sulphate-reducing bacteria [22,23]. Furthermore, the sulphate-reducing and methanogenesis bacteria actions are reflected by the increasing concentration of Pb, averaging 32.75 ppm. The reduction processes were observed in the studied samples but at a low rate indicated by the lower value of Ba and Pb concentration. The concentrations of Zn and Cu of the Madzaringwe showed, but zirconium, Zr (314.58–341.73 ppm) and vanadium showed a higher concentration (150.94–156.69 ppm). This higher concentration of Zr and V suggest an increasing paleo-productivity of organic matter and brackish deposit [24–26]. The average geochemical proxies ratio of V/(V + Ni) and V/Ni for all studied samples exceed 0.54 and 2.50 ppm, respectively, suggesting an anoxic condition of the depositional environment [8,27].

Table 2. Trace elemental composition of the Madzaringwe shale samples.

| Sample | Sc | V | Cr | Co | Ni | Cu | Zn | Rb | Sr | Y | Zr | Nb | Mo | Cs | Ba | La | Ce | Pr | Nd | Ni/Co |
|--------|-------|--------|-------|------|-------|-------|-------|-------|--------|-------|--------|-------|-------|-------|--------|------------|--------|-----------|--------|-------|
| SD1 | 25.19 | 151.88 | 82.80 | 5.51 | 45.09 | 43.09 | 65.30 | 69.77 | 328.15 | 56.63 | 314.58 | 29.64 | 1.37 | 9.15 | 557.17 | 91.48 | 168.57 | 19.27 | 63.60 | 8.18 |
| SD2 | 25.91 | 153.51 | 83.96 | 5.89 | 51.29 | 77.11 | 64.17 | 69.65 | 344.91 | 57.09 | 328.64 | 32.17 | 1.95 | 9.68 | 547.99 | 93.19 | 172.81 | 19.43 | 67.04 | 8.71 |
| SD3 | 23.44 | 150.94 | 73.08 | 5.34 | 39.04 | 39.92 | 65.37 | 67.69 | 336.77 | 53.99 | 317.59 | 28.83 | 1.87 | 9.76 | 550.62 | 91.01 | 170.72 | 19.21 | 64.11 | 7.31 |
| SD4 | 25.40 | 156.69 | 76.64 | 5.16 | 39.53 | 29.04 | 59.03 | 68.58 | 335.61 | 56.71 | 325.10 | 29.21 | 1.95 | 9.21 | 560.83 | 93.05 | 173.01 | 19.35 | 63.31 | 7.66 |
| SD5 | 25.22 | 156.61 | 78.22 | 5.96 | 43.54 | 39.45 | 57.46 | 70.11 | 325.77 | 58.22 | 315.47 | 29.52 | 1.89 | 9.32 | 527.61 | 92.60 | 170.34 | 19.62 | 66.19 | 7.31 |
| SD6 | 25.39 | 155.86 | 81.64 | 5.93 | 48.40 | 44.27 | 62.05 | 68.06 | 340.61 | 55.66 | 316.38 | 30.08 | 1.90 | 9.92 | 513.85 | 91.71 | 164.63 | 18.33 | 64.44 | 8.16 |
| SD7 | 25.09 | 156.88 | 86.66 | 5.79 | 45.75 | 37.30 | 58.51 | 73.87 | 343.57 | 59.75 | 341.73 | 31.51 | 2.27 | 9.65 | 560.88 | 93.34 | 173.39 | 19.40 | 64.70 | 7.90 |
| SD8 | 25.82 | 153.66 | 80.84 | 6.03 | 44.29 | 36.21 | 67.09 | 68.00 | 342.15 | 57.76 | 319.57 | 30.33 | 1.93 | 9.61 | 550.97 | 93.58 | 168.96 | 19.28 | 63.59 | 7.34 |
| SD9 | 23.49 | 155.09 | 85.37 | 5.49 | 43.44 | 37.23 | 59.86 | 68.15 | 339.71 | 58.51 | 328.14 | 30.40 | 1.57 | 9.50 | 554.09 | 92.30 | 175.01 | 19.51 | 63.83 | 7.91 |
| SD10 | 23.45 | 156.02 | 85.12 | 4.85 | 39.50 | 33.12 | 61.89 | 73.00 | 333.74 | 56.50 | 316.50 | 30.53 | 1.97 | 9.55 | 533.70 | 88.48 | 174.55 | 19.61 | 61.87 | 8.14 |
| Contd | Sm | Eu | Gd | Tb | Dy | Ho | Er | Tm | Yb | Lu | Hf | Ta | Pb | Th | U | V/(V + Ni) | V/Cr | (Eu/Eu *) | (Ce *) | U/Th |
| SD1 | 12.14 | 2.57 | 10.75 | 1.57 | 9.49 | 2.07 | 4.87 | 0.72 | 5.30 | 0.76 | 8.73 | 2.01 | 30.62 | 29.52 | 6.67 | 0.77 | 3.37 | 0.05 | 14.44 | 0.23 |
| SD2 | 12.99 | 2.47 | 10.47 | 1.50 | 9.16 | 1.95 | 5.31 | 0.83 | 5.13 | 0.78 | 7.70 | 2.20 | 35.22 | 30.58 | 6.73 | 0.75 | 2.99 | 0.05 | 14.62 | 0.22 |
| SD3 | 12.92 | 2.44 | 10.69 | 1.55 | 9.27 | 1.95 | 5.06 | 0.79 | 4.90 | 0.78 | 8.23 | 2.14 | 35.11 | 29.85 | 6.45 | 0.79 | 3.87 | 0.05 | 14.54 | 0.22 |
| SD4 | 13.28 | 2.50 | 10.85 | 1.76 | 9.51 | 2.09 | 5.39 | 0.93 | 6.00 | 0.79 | 8.14 | 2.11 | 33.49 | 31.76 | 6.47 | 0.80 | 3.96 | 0.05 | 14.63 | 0.20 |
| SD5 | 12.53 | 2.20 | 11.94 | 1.72 | 9.69 | 1.99 | 5.14 | 0.79 | 5.49 | 0.68 | 8.11 | 2.14 | 32.55 | 30.63 | 6.65 | 0.78 | 3.60 | 0.04 | 14.52 | 0.22 |
| SD6 | 12.75 | 2.27 | 11.01 | 1.64 | 9.55 | 1.99 | 5.25 | 0.77 | 4.49 | 0.77 | 8.07 | 2.02 | 33.74 | 29.44 | 6.35 | 0.76 | 3.22 | 0.04 | 14.27 | 0.22 |
| SD7 | 14.06 | 2.24 | 10.76 | 1.69 | 9.75 | 2.00 | 4.95 | 0.77 | 5.31 | 0.85 | 7.81 | 2.18 | 31.95 | 31.88 | 6.65 | 0.77 | 3.43 | 0.04 | 14.65 | 0.21 |
| SD8 | 12.28 | 2.48 | 11.76 | 1.68 | 10.13 | 1.96 | 5.42 | 0.83 | 5.68 | 0.86 | 8.23 | 2.11 | 32.13 | 30.59 | 6.33 | 0.78 | 3.47 | 0.05 | 14.46 | 0.21 |
| SD9 | 13.55 | 2.20 | 10.48 | 1.74 | 9.13 | 1.89 | 5.42 | 0.84 | 5.10 | 0.80 | 8.44 | 2.13 | 32.98 | 29.26 | 6.53 | 0.78 | 3.57 | 0.04 | 14.72 | 0.22 |
| SD10 | 13.33 | 2.71 | 10.35 | 1.57 | 8.88 | 1.91 | 5.25 | 0.90 | 5.39 | 0.79 | 8.22 | 1.99 | 29.63 | 29.36 | 6.24 | 0.80 | 3.95 | 0.05 | 14.70 | 0.21 |

* denotes Upper Continental Crust (UCC) values equivalents.

In addition, the siderophile and sulphurophile elemental proxies of the U/Th, Ni/Co, and V/(V + Ni) plot shown in Figure 3a,b depict anoxic redox conditions. This environment indicates reducing H₂S, which is necessary for preserving organic matter during methanogenesis processes [28]. This interpretation is consistent with black shale in North America that showed V/(V + Ni) ≥ 0.54, indicating anoxic environments.

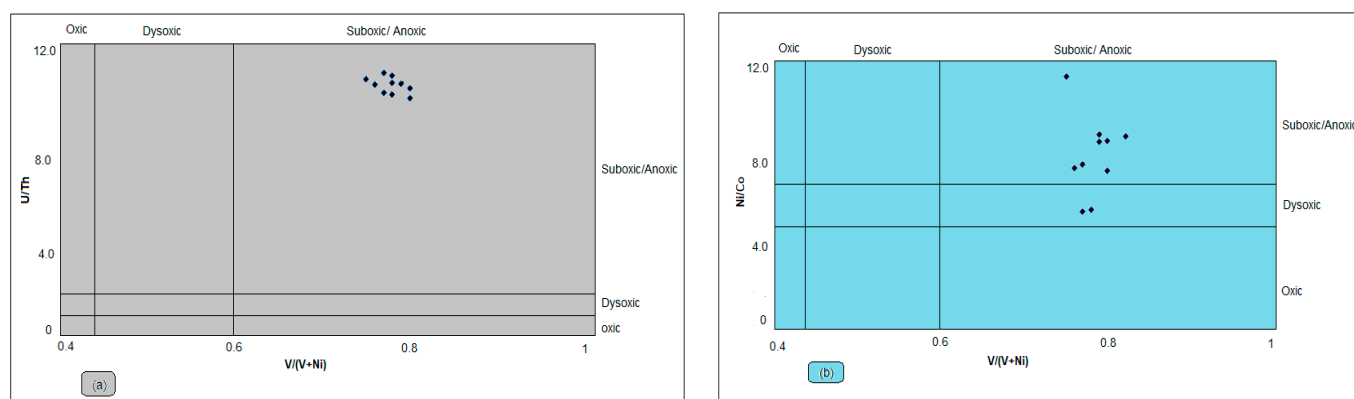


Figure 3. Geochemical proxies (a) $V/(V + Ni)$ vs U/Th (b) $v/(v + Ni)$ vs Ni/Co after [27].

The micro-FTIR spectra of the studied carbonaceous shale depict different organic and mineral content absorbance bands at various diagnostic wavelengths of the infrared spectrum (Figure 3). Due to C–H stretching vibrations, hydrocarbons show infrared absorption peaks between 2800 and 3300 cm^{-1} . The aromatic compounds of the organic matter show absorption peaks between 550 to 1200 cm^{-1} . Most of the studied samples exhibit a strong characteristic absorbance peak around 650 and 900 cm^{-1} , corresponding to the aromatic phenolic group, C=C–OH. However, the wavelength peak reduces as temperature increase depth due to bond deformation. The aromatic C=C absorption suggests the wavelength band of detrital plant lignin-derivative materials, unlike the amide band prevalent for marine-derivative materials [29]. The peak stretching from around 1000 to 1220 cm^{-1} indicates the C–O stretching and OH deformation of the carboxylic, COOH groups are exhibited samples suggesting decarboxylation of organic matter. The deformation of the carboxylic group releases CO_2 , which is recognised for its characteristic strong absorptions around 2000 to 2300 cm^{-1} [30].

The carbon and oxygen isotopic compositions of organic materials associated with the carbonaceous shale samples of the Tuli Basin are presented in Table 3. The carbon isotopic composition, $\delta^{13}C$, of the organic-rich shales of the Madzaringwe Formation, ranged from values -21.01 to -24.0% , averaging at -22.4% . It implies that most carbon isotopic signatures of studied samples reflect provenance from terrigenous plant material since it exceeds the -22% value, as shown in Figure 4. Meanwhile, the carbon isotopic composition found with -20% values indicates some influx of organic materials from marine settings [31].

This interpretation is consistent with the $\delta^{13}C$ values of the Whitehill Formation of the main Karoo Basin found with mixed marine and terrigenous organic carbon material. This isotopic discrimination indicates higher land plants with vascular tissues to range from -22.4 to -23.1% (Figure 5), contrary to marine plants such as algae which have a lower isotopic signature of -30 to -27% . The interpretation of terrigenous plant source is consistent with isotopic fractions for carbonaceous Barakar Formation in India, ranging from -23 to -25% [32].

Table 3. Isotopic compositions of $\delta^{13}C$ and $\delta^{18}O$.

| Samples | SD1 | SD2 | SD3 | SD4 | SD5 | SD6 | SD7 | SD8 | SD9 | SD10 |
|--------------------|-------|--------|--------|-------|-------|-------|--------|--------|--------|--------|
| $\delta^{13}C$ (‰) | −22.4 | −22.08 | −22.04 | −23.1 | −24.0 | −22.5 | −23.02 | −22.01 | −21.15 | −21.06 |
| $\delta^{18}O$ (‰) | 9.80 | 9.45 | 9.82 | 9.96 | 9.75 | 9.94 | 9.89 | 9.87 | 9.76 | 9.95 |

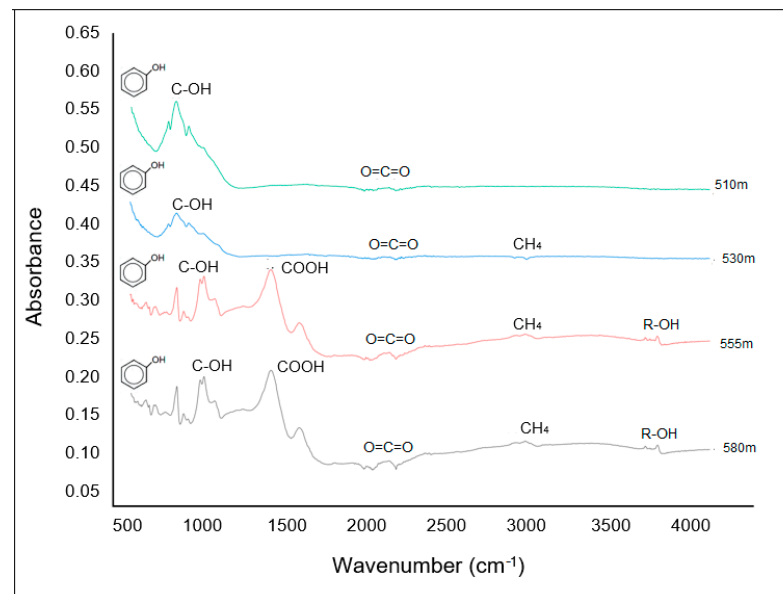


Figure 4. Micro-FTIR spectra are showing functional groups corresponding to organic molecules in studied shale.

In contrast, marine plants such as phytoplankton contribute carbon enrichment in a typical euxinic depositional environment with an average $\delta^{13}\text{C}$ value of around -30% [33]. Notably, the positive excursion of organic carbon isotopes $\delta^{13}\text{C}$ suggests local anoxia deposited about 280 Ma Permian period instead of the large-magnitude negative carbon isotope excursion close to the Ediacaran-Cambrian period [34]. During this period, a prolonged high burial rate of organic material led to global $\delta^{13}\text{C}$ enrichment in surface water, resulting in isotopically light CO_2 in basins [34].

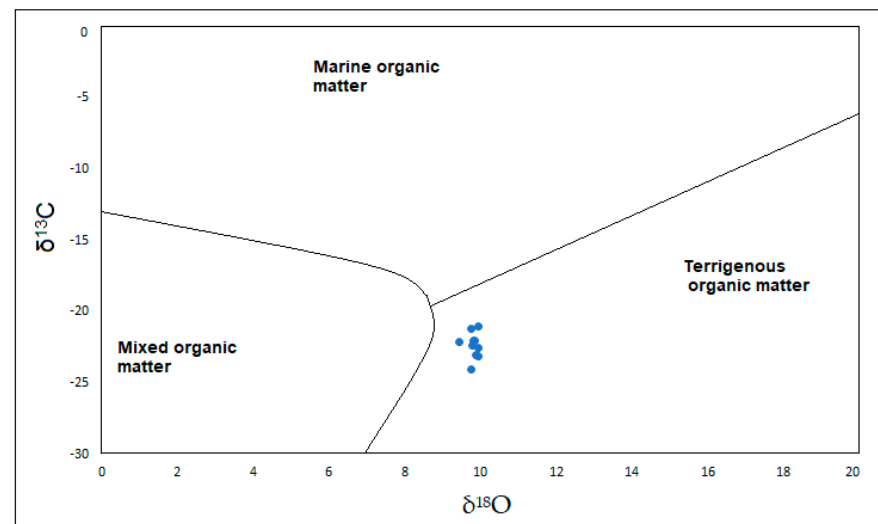


Figure 5. Cross-plot of $\delta^{18}\text{O}$ vs $\delta^{13}\text{C}$ values for the studied organic-rich shale modified after [35].

Meanwhile, isotopic composition, $\delta^{18}\text{O}$, tends to increase downward from 485 m to 580 m with intermittent anomalous depleted values. The increasing $\delta^{18}\text{O}$ values are attributed to a significant influx of meteoric water, while the anomalously depleted oxygen values show a decrease in pore-water $\delta^{18}\text{O}$ values during diagenesis of mineral–water interactions in a closed chemical microsystem of shale [36]. The negative correlation of $\delta^{18}\text{O}$ relate with degradation of organic matter content reflected in loss of ignition. The loss of ignition suggests combustion of the carbon content of land-derived organic matter, which

is rich in vascular plant materials. Such inference is consistent with the carbon isotopic compositions of the studied Madzaringwe shales, which show Type-III kerogen [35,37] in Figure 6. This interpretation agrees with the terrigenous source depicted by the plot of $\delta^{18}\text{O}$ vs $\delta^{13}\text{C}$ values. In contrast, the observed carbon isotopic composition of alum shale in southern Scandinavia is typical of marine sources varying from -30 to -27‰ , which mainly belong to the Type-I kerogen domain [31].

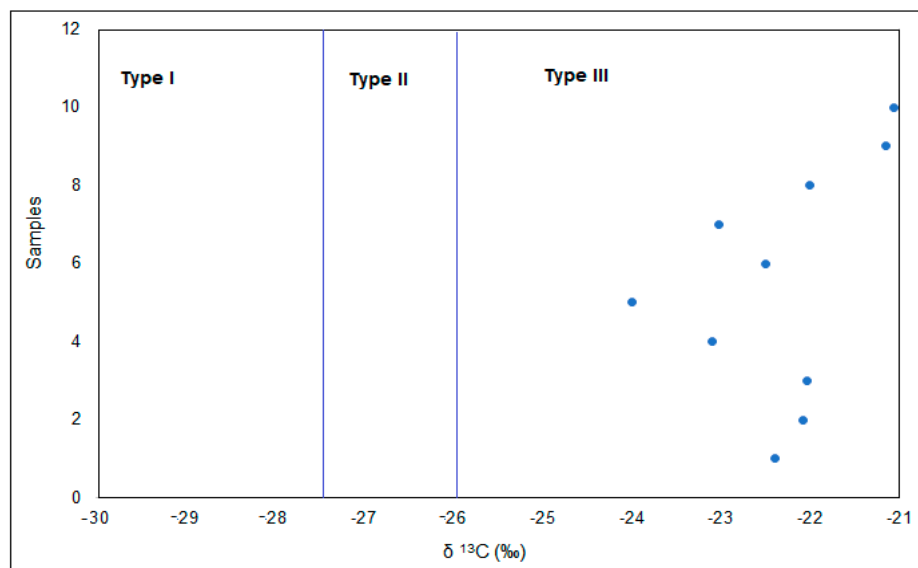


Figure 6. Carbon isotopic compositions of studied Madzaringwe samples show kerogen-type domains [37].

5. Discussion

5.1. Paleo-Redox Condition of the Depositional Environment

The oxides of Al and Ti elements have been used as a veritable tool to interpret deposited sediments due to their immobility nature during transportation from weathered source rock (McLennan et al., 2006, McLennan, 2001, Hayashi et al., 1997). The elemental proxies ratio of $\text{Al}_2\text{O}_3/\text{TiO}_2$ values ≥ 25 indicates sedimentary and intermediate igneous sources. The Index of Compositional Variation (ICV) of the carbonaceous shale samples has an average value of <0.1 , which is comparable with the Paleogene-Neogene black shales of Arang, Nyalau Tanjong Balingian Bergih Liang Formations in Malaysia enriched with kerogen capable of generating gas (Baiyegunhi et al., 2018). The elemental ratio $\text{K}_2\text{O}/\text{Al}_2\text{O}_3$ (0.03) of the studied samples showed values ≤ 0.5 , which suggests a highly mature shale since a significant amount of Al_2O_3 is typical of immature sediments (Cox et al., 1995). The plot (Figure 7) showed that the studied samples had both felsic and intermediate igneous provenances, thus explaining the higher values of alumina and silica [38].

Elemental proxies of trace elements have proven to be veritable tools for deciphering and discriminating paleo environments under which sedimentary deposits were formed due to their geochemical resilience to weathering, diagenesis, and sensitivity to redox reaction. Vanadium and Nickel exhibit similar geochemical behaviour and are considered to be highly stable organophilic and sulphur-forming elements [27,39]. The elemental ratio of $\text{V}/(\text{V} + \text{Ni})$ with a value greater than 0.5 has been interpreted to represent a reducing environment, with less than 0.5 as an oxidising environment [40,41].

Under this oxic condition, elements such as V, Ni, Fe, Mn, Mo, and sulphate are normally present in soluble species in the form of V^{5+} , Ni^{2+} , Fe^{3+} , Mn^{4+} , Mo^{6+} , and SO_4^{6+} , respectively, in the water column. At the same time, the aerobic degradation of organic matter continues until the dissolved oxygen is less than 0.2 mL/L H_2O [42]. Deficiency of oxygen has been adduced to climate, sea-level changes, tectonic activities, and hydrographic factors, resulting in insufficient oxygen supply to oxidise the organic

materials [43,44]. Below this oxygen concentration, anaerobic condition and degradation of organic matter begin and reduce the oxidising elements to insoluble species of V^{4+} , Ni, Fe^{2+} , Mn^{2+} , thiomolybdate oxyanion (MoO_4^{2-}) and SO_4^{2+} , which eventually concentrate in shale sediments [27].

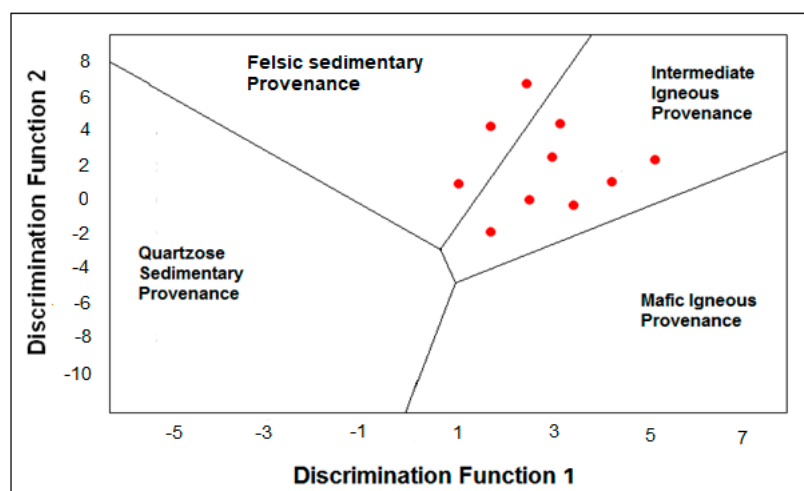


Figure 7. Plot of Discrimination functions using major elements index for felsic and mafic provenance and quartzose sedimentary provenance (Note: Discrimination Function 1: $-1.733 TiO_2 + 0.607 Al_2O_3 + 0.76 Fe_2O_3 (t) - 1.5 MgO + 0.616 CaO + 0.509 Na_2O - 1.224 K_2O - 0.909$. Discrimination Function 2: $0.445 TiO_2 + 0.07 Al_2O_3 - 0.25 Fe_2O_3 (t) - 1.142 MgO + 0.438 CaO + 1.475 Na_2O + 1.426 K_2O - 6.861$) [38].

The anoxic setting is established as all the oxidants in the shale sediments deplete due to further reduction processes relating to burial depth, thus promoting the activities of sulphide-reducing bacteria [45]. Studies [46–49] highlighted compounds such as hydrogen sulphide and zinc sulphide and iron sulphide as evidence of the reduction process ensued from sulphide-driven bacteria. With further increase in burial depth below the sediment–water interface, the methanogens begin to degrade the organic matter to generate biogenic methane. This explanation is consistent with the previous studies [27,50–53] which argued that methane is unlikely to form unless all sulphates are depleted while vanadium and nickel are concentrated.

5.2. Hydrothermal Activity and Paleo-Productivity

Some studies [54,55] have indicated that high amounts of Zn in shale rocks may be related to syn or post-depositional hydrothermal overprint. At the same time, elements such as Ni, Co, and Cu have been used to indicate hydrothermal overprint in shale formation during the initial stage of deposition [40,56,57]. In recent work [27], the diagram of Zn–Ni–Co has been used to determine the influence of hydrothermal activities on hydrocarbon sources (Figure 8). The average concentrations of elements Zn, Ni, Co, and Cu for the Madzaringwe shale are relatively higher, suggesting heating at depth and re-emergence at upper sedimentation. This slight hydrothermal influence might have emanated from the geothermal spring's temperatures ranging from 40–100 °C [58]. In Figure 7, the plot of the Zn, Ni, and Co thermometry elements shows heat influence from hydrothermal overprint. It is unlikely that the hydrothermal fluid could have permeated since shale has extremely low permeability and porosity [59]. Still, convection can transfer heat [60].

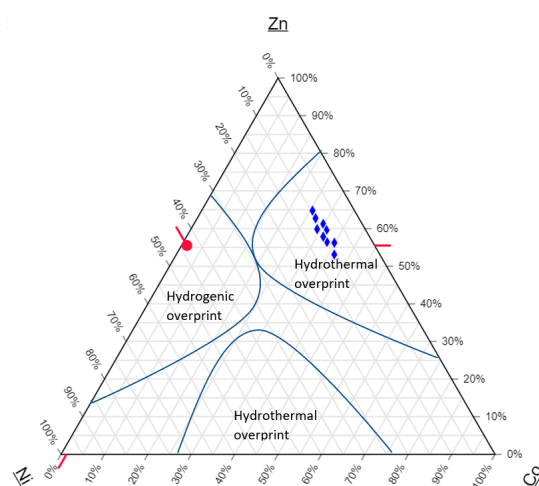


Figure 8. Zn-Ni-Co hydrothermal diagram of the represented studied shale samples [27].

Ba as a paleo-productivity indicator in sediments exposed to hydrothermal overprint seems unviable due to their susceptibility to alteration. However, the Ba concentration of the studied shales is relatively high, suggesting a non-marine environment since it exceeds the 400 ppm threshold for the marine environment in the Madzaringwe shale [61,62]. Implicitly, high detrital influx with low marine paleo-productivity characterises the studied shale, and this interpretation is consistent with the previous study [62], suggesting accumulation of land-derived plant material. To further corroborate the paleo-productivity condition, the Sr/Rb elemental proxy ratio in shale is mostly considered a veritable tool to interpret paleo-environmental settings due to their higher anionic radii and charges [63].

Following the Sr/Rb proxy, the studied shale samples indicate a significant amount of organic matter production from brackish water rather than marine, since brackish water represents a value greater than 0.6, while marine water is less than 0.6 [63].

5.3. Aliphatic Hydrocarbon Potentials

Due to C–H stretching vibrations, hydrocarbons show infrared absorption peaks between 2800 and 3300 cm^{-1} . The sp^2 C–H hybridisation found with an absorption peak between 3000–3100 cm^{-1} wavelength indicates the gaseous hydrocarbon. Some studies [64,65] reported the gaseous hydrocarbon of CH_4 has infrared absorbance peaks between 2850 and 3000 cm^{-1} due to aliphatic C–H stretching of methyl and methylene vibration, while the low absorption peak around 3500 cm^{-1} corresponds to water desorption wavelength [66]. In aromatic hydrocarbon, the carbon chain voids act as trapping and binding sites for organic lipids and inorganic materials such as hydrous oxides and clay minerals [67]. At greater burial depths around 510 and 580 m, the spectra showed inconspicuous peaks of the carboxylic group suggesting the maturation of organic matter beyond the methanogenesis window to coalification.

5.4. Stable Isotopic Signatures of an Anoxic Depositional Environment

The relative amounts of carbon and oxygen isotopic compositions of organic matter are a function of paleo-environmental deposition, which is significant to oil and gas exploration. In the studied carbonaceous Madzaringwe shale, the relationship between $\delta^{13}\text{C}$ and $\delta^{18}\text{O}$ of organic material suggests a bacterial reduction of organic compounds to CO_2 and hydrogen through an enzymatic reaction in the absence of sulphate. The significant role of reducing-bacterial involves converting the CO_2 and degradation of organic matter into new biomass. This reduction process increases the total organic carbon contents of sedimentary rocks through a biogenic origin [68,69]. Like the Madzaringwe shale, the Santa Barbara Basin in the United States has a biogenic source from a burial depth of less than 1000 m. This basin has been reported to have high total organic carbon contents that resulted from a biogenic mediation of chemoautotrophic and Beggiatoa

bacteria activities [70]. Furthermore, an organic isotopic study of the Qiongzhusi Formation in the Sichuan Basin revealed a high degree of total organic content generated by microbial bacteria [71]. Furthermore, the oxygen isotopic composition $\delta^{18}\text{O}$ of the studied organic matter has revealed a depleted oxygen value from 16.15‰ to 9.82‰, indicating a mixture of organic water with hydrothermal-meteoritic water conditions. This depleted oxygen favours the abundance of organic matter, indicating the redox condition of the water body from which the shale was deposited because organic matter can be preserved well in a strongly reducing environment.

5.5. Comparison of the Permian Madzaringwe Shale with Selected Permian Southern Gondwana Basin

The Madzaringwe shale of the Tuli Basin is geographically positioned in the southern Gondwana supercontinent having similar age as the Irati Formation in Parana Basin, Brazil [72,73], Bowen Formation in Australia [74,75], and Whitehill Formation in the main Karoo group, South Africa [76–78] during the Permian period (Figure 9). Recently, the age of the shale gas-bearing Irati Formation has been constrained using U-Pb zircon, indicating 275.75 ± 0.29 Ma corresponding to the Permian period [79]. The rapid evolutionary changes in land plants of Gondwana are attributable to the dramatic climatic change after the deglaciation of the Carboniferous Tshidzi fluvioglacial of the Tuli Basin [15], Dywka group of Karoo group [80,81], and Itararé sub-group of Paraná Basin [82,83]. On the other hand, the Tuli Basin differs from the mentioned southern Gondwana Basin based on non-marine sedimentation. The preservation of carbonaceous shale and coal seams is associated with a humid climate under autochthonous reducing conditions and deposited by fluvial activity in the depozones. The lithologies of the Tuli and the Gondwana Basins generally consist of diamictite with a clast ranging up to 2 m in diameter embedded in an argillaceous and sandy matrix [15,75,82] underlying the shale gas-bearing formations.

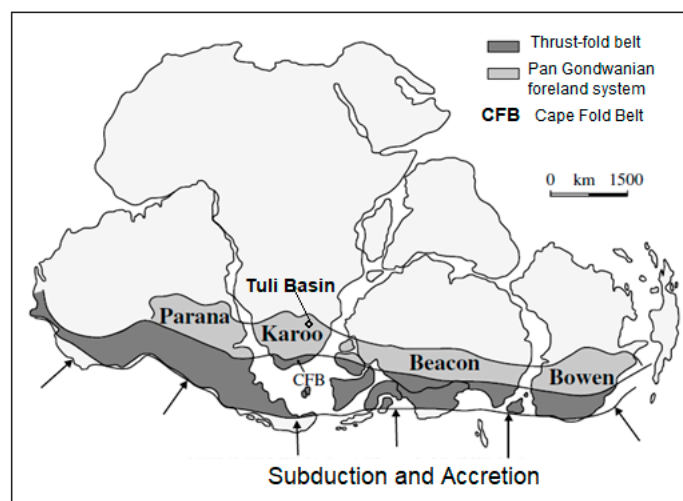


Figure 9. Paleogeographic reconstruction of the Southern Gondwana Permian Basins [78].

Plant fossils—“*Glossopteris Flora*” characterised the southern Gondwana Permian Basin of the Ecca group [16], Parana, Bowen [84], Beacon [85,86], and Tuli Basin [15]. Although evaluation of the Madzaringwe shale gas potential is in progress in South Africa, the Permian Whitehill Formation (South Africa) has a technically recoverable shale gas resource of 13–23 trillion cubic feet (Tcf) [76,77,87]. Based on the total organic carbon (TOC), which ranged from 2.57–6.90 wt%, the Whitehill Formation can be considered a good to excellent shale gas potential source. However, the source rock is thermally overmatured because the vitrinite reflectance exceeds 3% R_o , but still capable of generating shale gas such as the Marcellus shale of the Appalachian Basin [88,89]. In Australia, most shales and coals within the Bowen Basin have source rock potential [75] as well as the Irati and Rio Bonito

Formation in Brazil, which host shale and coal source rock, respectively. Furthermore, the gas potential in the Taroom and Denison Troughs is reported to be dominated by Type III kerogen, which is gas-prone [90].

6. Conclusions

Stable carbon and oxygen isotopes, functional groups and geochemical compositions have been a veritable tool to decipher the provenance of organic-rich shale with implications for potential gas generation. Organic rich shale emanating from a terrigenous anoxic paleo-environment indicates Type-III kerogen under sufficient thermal maturity. Terrigenous organic materials were preserved in a reducing condition, having a significant amount of organic matter production from brackish water. The stable isotopic and functional group of organic rich shale reveal the predominance of land-derived vascular plant materials. Meanwhile, the infrared spectra of the studied carbonaceous shale depict characteristic absorbance wavelengths corresponding to the aliphatic hydrocarbon functional group.

Author Contributions: The conceptualisation and writing of the original manuscript were conducted by G.O.A.; project administration and supervision by F.A.-D., S.R., S.E.M.; formal analysis and methodology by G.O.A.; resources, data curation, and software by S.E.M. All authors have read and agreed to the published version of the manuscript.

Funding: This research received no external funding.

Acknowledgments: The authors are grateful for the assistance provided by Ally Mahlaule during the data collections.

Conflicts of Interest: The authors declare no conflict of interest.

References

1. Agrawal, V.; Sharma, S. Molecular characterization of kerogen and its implications for determining hydrocarbon potential, organic matter sources and thermal maturity in Marcellus Shale. *Fuel* **2018**, *228*, 429–437. [[CrossRef](#)]
2. Wei, L.; Wang, Y.; Mastalerz, M. Comparative optical properties of macerals and statistical evaluation of mis-identification of vitrinite and solid bitumen from early mature Middle Devonian–Lower Mississippian New Albany Shale: Implications for thermal maturity assessment. *Int. J. Coal Geol.* **2016**, *168*, 222–236.
3. Sun, C.; Nie, H.; Dang, W.; Chen, Q.; Zhang, G.; Li, W.; Lu, Z. Shale gas exploration and development in China: Current status, geological challenges, and future directions. *Energy Fuels* **2021**, *35*, 6359–6379. [[CrossRef](#)]
4. Qiao, J.; Baniasad, A.; Zieger, L.; Zhang, C.; Luo, Q.; Littke, R. Paleo-depositional environment, origin and characteristics of organic matter of the Triassic Chang 7 Member of the Yanchang Formation throughout the mid-western part of the Ordos Basin, China. *Int. J. Coal Geol.* **2021**, *237*, 103636. [[CrossRef](#)]
5. Hakimi, M.H.; Abdullah, W.H.; Alqudah, M.; Makeen, Y.M.; Mustapha, K.A. Organic geochemical and petrographic characteristics of the oil shales in the Lajjun area, Central Jordan: Origin of organic matter input and preservation conditions. *Fuel* **2016**, *181*, 34–45. [[CrossRef](#)]
6. Małachowska, A.; Lis, G.; Mastalerz, M.; Goodarzi, F.; Sanei, H. The effect of paleo-environment on hydrocarbon generation potential: Example from Vaca Muerta Formation, Neuquén Basin, Argentina. *J. Pet. Sci. Eng.* **2022**, *208*, 109342. [[CrossRef](#)]
7. Zhao, W.; Wen, Z.; Zhang, H.; Wu, C.; Liu, Y.; Song, H.; Zhang, L.; Xi, Y.; Sun, L. Integrated Assessment of Marine-Continental Transitional Facies Shale Gas of the Carboniferous Benxi Formation in the Eastern Ordos Basin. *Energies* **2021**, *14*, 8500. [[CrossRef](#)]
8. Liang, C.; Jiang, Z.; Cao, Y.; Zhang, J.; Guo, L. Sedimentary characteristics and paleoenvironment of shale in the Wufeng-Longmaxi Formation, North Guizhou Province, and its shale gas potential. *J. Earth Sci.* **2017**, *28*, 1020–1031. [[CrossRef](#)]
9. Wang, S.; Zhao, W.; Zou, C.; Dong, D.; Wang, Y.; Li, X.; Guan, Q. Organic carbon and stable CO isotopic study of the Lower Silurian Longmaxi Formation black shales in Sichuan Basin, SW China: Paleoenvironmental and shale gas implications. *Energy Explor. Exploit.* **2015**, *33*, 439–457. [[CrossRef](#)]
10. Wright, M.; Mu, G.; Wang, S.; Liu, B.; Davies, E.; Singh, N. Chemostratigraphy and Sequence Stratigraphic Investigation of the Lower Silurian–Upper Ordovician Hot Shale, Southeastern of the Sichuan Basin. In Proceedings of the SPE Unconventional Resources Conference and Exhibition-Asia Pacific, Brisbane, Australia, 11–13 November 2013.
11. Bordy, E.M.; Catuneanu, O. Sedimentology of the Beaufort-Molteno Karoo fluvial strata in the Tuli Basin, South Africa. *S. Afr. J. Geol.* **2002**, *105*, 51–66.
12. Johnson, M.; Van Vuuren, C.; Hegenberger, W.; Key, R.; Show, U. Stratigraphy of the Karoo Supergroup in southern Africa: An overview. *J. Afr. Earth Sci.* **1996**, *23*, 3–15. [[CrossRef](#)]
13. Burke, K.; Dewey, J. Plume-generated triple junctions: Key indicators in applying plate tectonics to old rocks. *J. Geol.* **1973**, *81*, 406–433. [[CrossRef](#)]

14. Bordy, E.M.; Catuneanu, O. Sedimentology and palaeontology of upper Karoo aeolian strata (Early Jurassic) in the Tuli Basin, South Africa. *J. Afr. Earth Sci.* **2002**, *35*, 301–314. [[CrossRef](#)]
15. Chidley, C. *The Geology of the Country around Evangelina and Pontdrift (1: 50,000 Sheets 2228BD and 2229A)*; Unpublished South African Geological Survey Report; South Africa Geological Survey: Johannesburg, South Africa, 1985.
16. Johnson, M.; Anhaeuser, C.; Thomas, R.J. *The Geology of South Africa*; Geological Society of South Africa: Johannesburg, South Africa, 2006; pp. 490–491, ISBN1 1-919908-77-3, ISBN2 978-1-919908-77-9.
17. Ortlepp, G. Limpopo Coalfield. Mineral Deposits of Southern Africa. Ph.D. Thesis, Rhodes University, Grahamstown, Eastern Cape Province, South Africa, 1986.
18. Mtinkulu, M.N. *A Provisional Basinal Study of the Waterberg-Karoo*; University of Pretoria: Pretoria, South Africa, 2010.
19. Bordy, E.M. Sedimentology of The Karoo Supergroup in The Tuli Basin. Ph.D. Thesis, Rhodes University, Grahamstown, Eastern Cape Province, South Africa, 2000. (Unpublished)
20. Lebena, K.; Möttele, R.; Paavera, P.; Konistb, A.; Kalle Kirsimäe, T.P. Geochemical study of stable carbon and oxygen isotopes in landfilled Carich oil shale ash. *Est. J. Earth Sci.* **2020**, *69*, 134–142. [[CrossRef](#)]
21. Mesquita, C.J.S.; Dall’Agnol, R.; Almeida, J.d.A.C.d. Mineral chemistry and crystallization parameters of the A-type Paleoproterozoic Bannach granite, Carajás province, Pará, Brazil. *Braz. J. Geol.* **2018**, *48*, 575–601. [[CrossRef](#)]
22. Hanor, J.S. Barite–celestine geochemistry and environments of formation. *Rev. Mineral. Geochem.* **2000**, *40*, 193–275. [[CrossRef](#)]
23. Saba, T. Hydraulic Fracturing: Data Analysis Methods to Identify Sources of Dissolved Gas and Chemical Compounds in Drinking Water Wells. In *Introduction to Environmental Forensics*; Elsevier: Amsterdam, The Netherlands, 2015; pp. 513–529.
24. Li, Y.; Zhang, T.; Ellis, G.S.; Shao, D. Depositional environment and organic matter accumulation of Upper Ordovician–Lower Silurian marine shale in the Upper Yangtze Platform, South China. *Palaeogeogr. Palaeoclimatol. Palaeoecol.* **2017**, *466*, 252–264. [[CrossRef](#)]
25. Wu, C.; Tuo, J.; Zhang, M.; Liu, Y.; Xing, L.; Gong, J.; Qiu, J. Multiple controlling factors of lower Palaeozoic organic-rich marine shales in the Sichuan Basin, China: Evidence from minerals and trace elements. *Energy Explor. Exploit.* **2017**, *35*, 627–644. [[CrossRef](#)]
26. Frapé, S.K.; Blyth, A.; Blomqvist, R.; McNutt, R.H.; Gascoyne, M. Deep Fluids in Continents: II Crystalline Rocks. In *Surface and Groundwater, Weathering, and Soils, Vol. 5. Treatise on Geochemistry*; Drever, J.I., Ed.; Elsevier-Pergamon: Oxford, UK, 2003.
27. Ferriday, T.; Montenari, M. Chemostratigraphy and Chemofacies of Source Rock Analogues: A High-Resolution Analysis of Black Shale Successions from the Lower Silurian Formigoso Formation (Cantabrian Mountains, NW Spain). In *Stratigraphy & Timescales*; Elsevier: Amsterdam, The Netherlands, 2016; pp. 123–255.
28. Akintola, G.O.; Amponsah-Dacosta, F.; Rupprecht, S.; Palaniandy, N.; Mhlongo, S.E.; Gitari, W.M.; Edokpayi, J.N. Methanogenesis Potentials: Insights from Mineralogical Diagenesis, SEM and FTIR Features of the Permian Mikambeni Shale of the Tuli Basin, Limpopo Province of South Africa. *Minerals* **2021**, *11*, 651. [[CrossRef](#)]
29. Naseem, A.; Tabasum, S.; Zia, K.M.; Zuber, M.; Ali, M.; Noreen, A. Lignin-derivatives based polymers, blends and composites: A review. *Int. J. Biol. Macromol.* **2016**, *93*, 296–313. [[CrossRef](#)]
30. Washburn, K.E.; Birdwell, J.E. Multivariate analysis of ATR-FTIR spectra for assessment of oil shale organic geochemical properties. *Org. Geochem.* **2013**, *63*, 1–7. [[CrossRef](#)]
31. Buchardt, B.; Clausen, J.; Thomsen, E. Carbon isotope composition of Lower Palaeozoic kerogen: Effects of maturation. *Org. Geochem.* **1986**, *10*, 127–134. [[CrossRef](#)]
32. Singh, P.K.; Singh, M.; Prachiti, P.; Kalpana, M.; Manikyamba, C.; Lakshminarayana, G.; Singh, A.K.; Naik, A. Petrographic characteristics and carbon isotopic composition of Permian coal: Implications on depositional environment of Sattupalli coalfield, Godavari Valley, India. *Int. J. Coal Geol.* **2012**, *90*, 34–42. [[CrossRef](#)]
33. Whiticar, M.J. Stable isotope geochemistry of coals, humic kerogens and related natural gases. *Int. J. Coal Geol.* **1996**, *32*, 191–215. [[CrossRef](#)]
34. Schröder, S.; Grotzinger, J. Evidence for anoxia at the Ediacaran–Cambrian boundary: The record of redox-sensitive trace elements and rare earth elements in Oman. *J. Geol. Soc.* **2007**, *164*, 175–187. [[CrossRef](#)]
35. Hu, J.; Huang, D. *The Foundation of China Continental Petroleum Geology Theory*; Petroleum Industry Press: Beijing, China, 1991.
36. Faure, K.; Harris, C.; Willis, J.P. A profound meteoric water influence on genesis in the Permian Waterberg Coalfield, South Africa; evidence from stable isotopes. *J. Sediment. Res.* **1995**, *65*, 605–613.
37. Sun, Z.; Wang, Y.; Wei, Z.; Zhang, M.; Wang, G.; Wang, Z. Characteristics and origin of desorption gas of the Permian Shanxi Formation shale in the Ordos Basin, China. *Energy Explor. Exploit.* **2017**, *35*, 792–806. [[CrossRef](#)]
38. Roser, B.P.; Korsch, R.J. Provenance signatures of sandstone-mudstone suites determined using discriminant function analysis of major-element data. *Chem. Geol.* **1988**, *67*, 119–139. [[CrossRef](#)]
39. Pieta, I.S.; Rathi, A.; Pieta, P.; Nowakowski, R.; Holdynski, M.; Pisarek, M.; Kaminska, A.; Gawande, M.B.; Zboril, R. Electrocatalytic methanol oxidation over Cu, Ni and bimetallic Cu-Ni nanoparticles supported on graphitic carbon nitride. *Appl. Catal. B Environ.* **2019**, *244*, 272–283. [[CrossRef](#)]
40. Hatch, J.; Leventhal, J. Relationship between inferred redox potential of the depositional environment and geochemistry of the Upper Pennsylvanian (Missourian) Stark Shale Member of the Dennis Limestone, Wabaunsee County, Kansas, USA. *Chem. Geol.* **1992**, *99*, 65–82. [[CrossRef](#)]

41. Tanwar, R.; Mandal, U.K. Photocatalytic activity of Ni_{0.5}Zn_{0.5}Fe₂O₄@ polyaniline decorated BiOCl for azo dye degradation under visible light—integrated role and degradation kinetics interpretation. *RSC Adv.* **2019**, *9*, 8977–8993. [[CrossRef](#)]
42. Tyson, R. *Sedimentary Organic Matter: Organic Facies and Palynofacies*; Springer Science & Business Media: Cham, Switzerland, 2012.
43. Dean, W.E.; Arthur, M.A. Iron-sulfur-carbon relationships in organic-carbon-rich sequences I: Cretaceous Western Interior Seaway. *Am. J. Sci.* **1989**, *289*, 708–743. [[CrossRef](#)]
44. Dar, S.A.; Khan, K.; Birch, W. Sedimentary: Phosphates. In *Reference Module in Earth Systems and Environmental Sciences*; Elsevier: Amsterdam, The Netherlands, 2017; Volume 10.
45. Capotondi, L.; Girone, A.; Lirer, F.; Bergami, C.; Verducci, M.; Vallefucio, M.; Afferri, A.; Ferraro, L.; Pelosi, N.; De Lange, G.J. Central Mediterranean Mid-Pleistocene paleoclimatic variability and its association with global climate. *Palaeogeogr. Palaeoclimatol. Palaeoecol.* **2016**, *442*, 72–83. [[CrossRef](#)]
46. Gallagher, S.J.; Kitamura, A.; Iryu, Y.; Itaki, T.; Koizumi, I.; Hoiles, P.W. The Pliocene to recent history of the Kuroshio and Tsushima Currents: A multi-proxy approach. *Prog. Earth Planet. Sci.* **2015**, *2*, 1–23. [[CrossRef](#)]
47. Sabino, M.; Schefuß, E.; Natalicchio, M.; Pierre, F.D.; Birgel, D.; Bortels, D.; Schnetger, B.; Peckmann, J. Climatic and hydrologic variability in the northern Mediterranean across the onset of the Messinian salinity crisis. *Palaeogeogr. Palaeoclimatol. Palaeoecol.* **2020**, *545*, 109632. [[CrossRef](#)]
48. Natalicchio, M.; Pierre, F.D.; Birgel, D.; Brumsack, H.; Carnevale, G.; Gennari, R.; Gier, S.; Lozar, F.; Pellegrino, L.; Sabino, M. Paleoenvironmental change in a precession-paced succession across the onset of the Messinian salinity crisis: Insight from element geochemistry and molecular fossils. *Palaeogeogr. Palaeoclimatol. Palaeoecol.* **2019**, *518*, 45–61. [[CrossRef](#)]
49. Reolid, M.; Duarte, L.; Rita, P. Changes in foraminiferal assemblages and environmental conditions during the T-OAE (Early Jurassic) in the northern Lusitanian Basin, Portugal. *Palaeogeogr. Palaeoclimatol. Palaeoecol.* **2019**, *520*, 30–43. [[CrossRef](#)]
50. Abanda, P.A.; Hannigan, R.E. Effect of diagenesis on trace element partitioning in shales. *Chem. Geol.* **2006**, *230*, 42–59. [[CrossRef](#)]
51. Algeo, T.J.; Maynard, J.B. Trace-element behavior and redox facies in core shales of Upper Pennsylvanian Kansas-type cyclothems. *Chem. Geol.* **2004**, *206*, 289–318. [[CrossRef](#)]
52. März, C.; Poulton, S.W.; Beckmann, B.; Küster, K.; Wagner, T.; Kasten, S. Redox sensitivity of P cycling during marine black shale formation: Dynamics of sulfidic and anoxic, non-sulfidic bottom waters. *Geochim. Cosmochim. Acta* **2008**, *72*, 3703–3717. [[CrossRef](#)]
53. Pi, D.-H.; Liu, C.-Q.; Shields-Zhou, G.A.; Jiang, S.-Y. Trace and rare earth element geochemistry of black shale and kerogen in the early Cambrian Niutitang Formation in Guizhou province, South China: Constraints for redox environments and origin of metal enrichments. *Precambrian Res.* **2013**, *225*, 218–229. [[CrossRef](#)]
54. Charriau, A.; Lesven, L.; Gao, Y.; Leermakers, M.; Baeyens, W.; Ouddane, B.; Billon, G. Trace metal behaviour in riverine sediments: Role of organic matter and sulfides. *Appl. Geochem.* **2011**, *26*, 80–90. [[CrossRef](#)]
55. Lipinski, M.; Warning, B.; Brumsack, H.-J. Trace metal signatures of Jurassic/Cretaceous black shales from the Norwegian Shelf and the Barents Sea. *Palaeogeogr. Palaeoclimatol. Palaeoecol.* **2003**, *190*, 459–475. [[CrossRef](#)]
56. Zhang, K.; Liu, R.; Liu, Z.; Li, B.; Han, J.; Zhao, K. Influence of volcanic and hydrothermal activity on organic matter enrichment in the Upper Triassic Yanchang Formation, southern Ordos Basin, Central China. *Mar. Pet. Geol.* **2020**, *112*, 104059. [[CrossRef](#)]
57. Yin, J.; Xu, C.; Hao, F.; Wang, Q.; Miao, Q.; Wang, Z.; Zou, H. Controls on organic matter enrichment in source rocks of the Shahejie Formation in the southwestern Bozhong Sag, Bohai Bay Basin, China. *Palaeogeogr. Palaeoclimatol. Palaeoecol.* **2020**, *560*, 110026. [[CrossRef](#)]
58. AE, T.; Olivier, J. Sagole Spa Resort, Current and Potential Uses. In Proceedings of the World Geothermal Congress, Bali, Indonesia, 25–29 April 2010; pp. 25–29.
59. Ren, J.; Guo, P.; Peng, S.; Yang, C. Investigation on permeability of shale matrix using the lattice Boltzmann method. *J. Nat. Gas Sci. Eng.* **2016**, *29*, 169–175. [[CrossRef](#)]
60. Raffensperger, J.P.; Vlassopoulos, D. The potential for free and mixed convection in sedimentary basins. *Hydrogeol. J.* **1999**, *7*, 505–520. [[CrossRef](#)]
61. Zhao, J.; Jin, Z.; Jin, Z.; Geng, Y.; Wen, X.; Yan, C. Applying sedimentary geochemical proxies for paleoenvironment interpretation of organic-rich shale deposition in the Sichuan Basin, China. *Int. J. Coal Geol.* **2016**, *163*, 52–71. [[CrossRef](#)]
62. Wen, H.; Zheng, R.; Tang, F.; Zheng, A.; Sang, T.; Chen, S.; Li, G.; Li, Z. Reconstruction and analysis of paleosalinity and paleoenvironment of the Chang 6 member in the Gengwan region, Ordos basin. *J. Mineral. Petrol.* **2008**, *28*, 114–120.
63. Zuo, X.; Li, C.; Zhang, J.; Ma, G.; Chen, P. Geochemical characteristics and depositional environment of the Shahejie Formation in the Binnan Oilfield, China. *J. Geophys. Eng.* **2020**, *17*, 539–551. [[CrossRef](#)]
64. Baker, M.J.; Trevisan, J.; Bassan, P.; Bhargava, R.; Butler, H.J.; Dorling, K.M.; Fielden, P.R.; Fogarty, S.W.; Fullwood, N.J.; Heys, K.A. Using Fourier transform IR spectroscopy to analyze biological materials. *Nat. Protoc.* **2014**, *9*, 1771. [[CrossRef](#)]
65. Günzler, H.; Gremlich, H.-U. IR Spectroscopy. An Introduction. Wiley-VCH: Weinheim, Germany, 2002; Volume 34, 374p.
66. Coenen, K.; Gallucci, F.; Mezari, B.; Hensen, E.; van Sint Annaland, M. An in-situ IR study on the adsorption of CO₂ and H₂O on hydrotalcites. *J. CO₂ Util.* **2018**, *24*, 228–239. [[CrossRef](#)]
67. Hillel, D.; Hatfield, J.L. *Encyclopedia of Soils in the Environment*; Elsevier: Amsterdam, The Netherlands, 2005; Volume 3.
68. Martini, A.M.; Budai, J.M.; Walter, L.M.; Schoell, M. Microbial generation of economic accumulations of methane within a shallow organic-rich shale. *Nature* **1996**, *383*, 155–158. [[CrossRef](#)]

69. Wang, H.; Xiao, E.; Li, Y.; Latif, K.; Riaz, M. New Advances and Existed Problems for the Forming Mechanism of the Microbial Dolomite. *sedimentology* **2018**, *2*, 5.
70. Li, C.; Sessions, A.L.; Kinnaman, F.S.; Valentine, D.L. Hydrogen-isotopic variability in lipids from Santa Barbara Basin sediments. *Geochim. Cosmochim. Acta* **2009**, *73*, 4803–4823. [[CrossRef](#)]
71. Wang, N.; Wen, L.; Li, M.; Dai, X.; Xu, Y.; Ming, Y.; Yang, S. The origin of abnormally ¹³C-depleted organic carbon isotope signatures in the early Cambrian Yangtze Platform. *Mar. Pet. Geol.* **2021**, *128*, 105051. [[CrossRef](#)]
72. Cassel, M.C.; Lavina, E.L.; Cagliari, J.; Rodrigues, R.; Pereira, E. Anoxia and salinity changes: A new Permian catastrophe record. *Clim. Past Discuss.* **2019**, *46*, 1–20.
73. dos Reis, D.E.; Rodrigues, R.; Moldowan, J.M.; Jones, C.M.; Brito, M.; da Costa Cavalcante, D.; Portela, H.A. Biomarkers stratigraphy of Irati Formation (lower permian) in the southern portion of Paraná Basin (Brazil). *Mar. Pet. Geol.* **2018**, *95*, 110–138. [[CrossRef](#)]
74. Dixon, D.A.; Pope, G.J. Oil shale of the Duaringa Basin, Central Queensland. *Fuel* **1987**, *66*, 305–308. [[CrossRef](#)]
75. Alison, T. *Petroleum Plays of the Bowen and Surat Basins Summary*; Australian Society of Exploration Geophysicist: Sydney, Australia, 2018; Volume 20, p. 3676.
76. De Kock, M.O.; Beukes, N.J.; Adeniyi, E.O.; Cole, D.; Gotz, A.E.; Geel, C.; Ossa, F.-G. Deflating the shale gas potential of South Africa's Main Karoo basin. *S. Afr. J. Sci.* **2017**, *113*, 1–12. [[CrossRef](#)]
77. Geel, C.; Schulz, H.-M.; Booth, P.; deWit, M.; Horsfield, B. Shale gas characteristics of Permian black shales in South Africa: Results from recent drilling in the Ecca Group (Eastern Cape). *Energy Procedia* **2013**, *40*, 256–265. [[CrossRef](#)]
78. Catuneanu, O. Retroarc foreland systems—evolution through time. *J. Afr. Earth Sci.* **2004**, *38*, 225–242. [[CrossRef](#)]
79. Cagliari, J.; Serratt, H.; Cassel, M.C.; Schmitz, M.D.; Chemale Jr, F. New high-precision U-Pb zircon age of the Irati Formation (Paraná Basin) and implications for the timing of the Kungurian anoxic events recorded in southern Gondwana. *Gondwana Res.* **2022**, *107*, 134–145. [[CrossRef](#)]
80. Ruckwied, K.; Götz, A.E.; Jones, P. Palynological records of the Permian Ecca Group (South Africa): Utilizing climatic icehouse–greenhouse signals for cross basin correlations. *Palaeogeogr. Palaeoclimatol. Palaeoecol.* **2014**, *413*, 167–172. [[CrossRef](#)]
81. Stephenson, M.H. Permian palynostratigraphy: A global overview. *Geol. Soc. Lond. Spec. Publ.* **2018**, *450*, 321–347. [[CrossRef](#)]
82. Holz, M.; França, A.B.; Souza, P.A.; Iannuzzi, R.; Rohn, R. A stratigraphic chart of the Late Carboniferous/Permian succession of the eastern border of the Paraná Basin, Brazil, South America. *J. S. Am. Earth Sci.* **2010**, *29*, 381–399. [[CrossRef](#)]
83. Holz, M.; Souza, P.A.; Iannuzzi, R.; Fielding, C.R.; Frank, T.D.; Isbell, J.L. Sequence stratigraphy and biostratigraphy of the Late Carboniferous to Early Permian glacial succession (Itararé subgroup) at the eastern-southeastern margin of the Paraná Basin, Brazil. In *Resolving the Late Paleozoic Ice Age in Time and Space*; Special Paper; Geological Society of America: Boulder, CO, USA, 2008; pp. 115–129.
84. Souza, R.I.P.A. Floral succession in the lower permian deposits of the brazilian paraná basin: Anup-to-date overview. In *Nonmarine Permian: Bulletin*; New Mexico Museum of Natural History and Science: Albuquerque, NM, USA, 2005; Volume 30, p. 144.
85. Cúneo, N.R.; Isbell, J.; Taylor, E.L.; Taylor, T.N. The Glossopteris flora from Antarctica: Taphonomy and paleoecology. *Comptes Rendus XII ICC-P* **1993**, *2*, 13–40.
86. Tewari, R.; Chatterjee, S.; Agnihotri, D.; Pandita, S.K. Glossopteris flora in the Permian Weller Formation of Allan Hills, South Victoria Land, Antarctica: Implications for paleogeography, paleoclimatology, and biostratigraphic correlation. *Gondwana Res.* **2015**, *28*, 905–932. [[CrossRef](#)]
87. Geel, C.; De Wit, M.; Booth, P.; Schulz, H.; Horsfield, B. Palaeo-environment, diagenesis and characteristics of Permian black shales in the Lower Karoo Supergroup flanking the Cape Fold Belt near Jansenville, eastern Cape, South Africa: Implications for the shale gas potential of the Karoo Basin. *S. Afr. J. Geol.* **2015**, *118*, 249–274. [[CrossRef](#)]
88. Zagorski, W.A.; Wrightstone, G.R.; Bowman, D.C. The Appalachian Basin Marcellus Gas Play: Its History of Development, Geologic Controls on Production, and Future Potential as a World-class Reservoir. In *Shale Reservoirs: Giant Resources for the 21st Century*; American Association of Petroleum Geologists (AAPG): Tulsa, OK, USA, 2012; pp. 172–200. [[CrossRef](#)]
89. Chabalala, V.P.; Wagner, N.; Malumbazo, N.; Eble, C.F. Geochemistry and organic petrology of the permian whitehill formation, Karoo Basin (RSA) and the Devonian/Carboniferous shale of the Appalachian Basin (USA). *Int. J. Coal Geol.* **2020**, *232*, 103612. [[CrossRef](#)]
90. Anthony, D. *A Review of Recent Conventional Petroleum Exploration and In-Field Gas Reserves Growth in the Denison Trough, Queensland*; Petroleum Exploration Society of Australia Inc.: Queensland, Australia, 2004.